

Anisotropic spin Hall and spin Nernst effects in bismuth semimetal

Guang-Yu Guo^{1,2,*}

¹*Department of Physics, National Taiwan University, Taipei 10617, Taiwan*

²*Physics Division, National Center for Theoretical Sciences, Taipei 10617, Taiwan*

(Dated: September 7, 2022)

Bismuth is an archetypal semimetal with gigantic spin-orbit coupling and it has been a major source material for the discovery of seminal phenomena in solid state physics for more than a century. In recent years, spin current transports in bismuth have also attracted considerable attention. In this paper, we theoretically study both spin Hall effect (SHE) and spin Nernst effect (SNE) in bismuth, based on relativistic band structure calculations. First, we find that there are three independent tensor elements of spin Hall conductivity (SHC) (σ_{ij}^s) and spin Nernst conductivity (SNC) (α_{ij}^s), namely, Z_{yx}^z , Z_{xz}^y , and Z_{zy}^x , where $Z = \sigma$ or α . We calculate all the elements as a function of the Fermi energy. Second, we find that all SHC elements are large, being ~ 1000 (\hbar/e)(S/cm). Furthermore, because of its low electrical conductivity, the spin Hall angles are gigantic, being ~ 20 %. Third, all the calculated SNC elements are also pronounced, being comparable to that [~ 0.13 (\hbar/e)(A/m-K)] of gold. Finally, in contrast to Pt and Au where $Z_{yx}^z = Z_{xz}^y = Z_{zy}^x$, the SHE and SNE in bismuth are anisotropic, i.e., $Z_{yx}^z \neq Z_{xz}^y \neq Z_{zy}^x$. In particular, SNC is highly anisotropic, and α_{yx}^z , α_{xz}^y and α_{zy}^x differ even in sign. Also, such anisotropy in SHE can be significantly enhanced by either electron or hole doping. Consequently, the Hall voltages due to the inverse SHE and inverse SNE from the different conductivity elements could cancel each other and thus result in a small spin Hall angle if polycrystalline samples are used, which may explain why the measured spin Hall angles ranging from nearly 0 to 25 % have been reported. We hope that these interesting findings would stimulate further experiments on bismuth using highly oriented single crystal specimens.

I. INTRODUCTION

In the past two decades, spin transport electronics (spintronics) has attracted considerable attention because of its promising applications in data storage and processing and other electronic technologies. Spin current generation, detection and manipulation are key issues in spintronics. Spin Hall effect (SHE), first proposed in 1971 [1], refers to the transverse spin current generation in a nonmagnetic solid with relativistic spin-orbit coupling (SOC) by an electric field [1–14]. It offers a rather unique method for pure spin current generation and manipulation without the need of an applied magnetic field or a magnetic material. Large SHE has been predicted and also observed in 5d transition metals such as platinum and tungsten with strong SOC [9–14]. In the inverse SHE [7], pure spin current is converted into a transverse charge current in a material with large SOC. ISHE has been widely used to detect spin currents [7, 8, 13, 14]. Similarly, pure transverse spin current could also be generated in a solid by applying a temperature gradient (∇T) rather than an electric field [15]. This thermally driven spin current generation is called spin Nernst effect (SNE) [15] and would make spintronics powered by heat possible, thus opening a new field known as spin caloritronics [16]. Large SNE has been recently observed in such materials as Pt film [17] and tungsten metal [18].

Bismuth (Bi) crystallizes in a rhombohedral $R\bar{3}m$ structure at ambient conditions [19] and is an archety-

pal semimetal [20, 21]. Bismuth is the heaviest nonradioactive element in the periodic table, and thus Bi has a gigantic SOC effect [21] (see also Fig. 1 below). For more than a century, Bi has been a key source material for the discovery of important phenomena in solid state physics, such as the large thermoelectric effect [20, 22], the largest Hall coefficient and highest magnetoresistance [23, 24]. The latter two unusual properties have been attributed to the large SOC in Bi [25]. More recently, Bi has also been found to host intrinsic superconductivity [26] and to be a higher order topological insulator [27] and also a rotational symmetry protected topological crystalline insulator [28]. Because of its strong SOC, one would expect bismuth to exhibit large SHE and SNE. Indeed, the contribution of the electron carriers to the spin Hall conductivity (SHC) in bismuth has been studied by model Dirac Hamiltonian and also anisotropic Wolff Hamiltonian [29–32] and the SHC was estimated to be two-orders of magnitude larger than that of Pt at room temperature. Furthermore, large SHC of ~ 470 (\hbar/e)(S/cm) in Bi was predicted by a realistic tight-binding Hamiltonian calculation [33], which is about one quarter of that of platinum [10]. Since bismuth is a semimetal with the electrical conductivity being much lower than that of platinum [20], one would expect bismuth to have a very large spin Hall angle (Θ_{sH}) (the ratio of the spin current to the longitudinal charge current, i.e., charge-spin conversion efficiency). Therefore, many investigations on spin current phenomena in Bi semimetal systems have been carried [34–39] and indeed large spin Hall angles of about 10 % have been reported in some of these experiments [34].

However, the magnitude of the reported Θ_{sH} values

* gyguo@phys.ntu.edu.tw

varies from zero (negligibly small) to 24 %, depending on the spin current detection method and also the magnetic material used to inject spin current in the experiments [38]. Moreover, the signs of the reported Θ_{sH} values could also differ. This unsatisfying state of the matter is partly due to the fact that apart from the SHE, spin current can also be generated by other means such as spin pumping at ferromagnetic resonance, SNE, lateral spin valve and longitudinal spin Seebeck effect (see [37] and references therein). On the other hand, we notice that the SHC (and also spin Nernst conductivity) for a solid is a third-order tensor and thus has 27 matrix elements. Of course, many of the elements are zero due to the crystalline symmetry constraints. For example, bcc W and fcc Pt has only one independent nonzero element (σ_{yx}^z). Nevertheless, it was reported that for hcp metals, there are two independent elements (σ_{yx}^z and σ_{xz}^y) [40]. These hcp metals could exhibit large anisotropic SHE if σ_{yx}^z and σ_{xz}^y differ considerably, e.g., in hcp Sc, hcp Zn and hcp Zr [40]. Consequently, the Hall voltages generated by the inverse SHE due to different SHC tensor elements could partially cancel each other and hence may result in an averaged smaller Θ_{sH} value if polycrystalline samples are used in the experiments. As will be discussed below in Sec. II B, rhombohedral bismuth has 4 independent nonzero elements (σ_{yx}^z , σ_{xz}^y , σ_{zy}^x and σ_{xx}^y) (see Table I below). However, only σ_{yx}^z of bismuth was reported in [33]. Clearly, the knowledge of all the four independent SHC tensor elements would help understand the wide spectrum of the reported Θ_{sH} values and also guide the development of spintronic devices using Bi semimetal.

Because of its semimetallic nature, the thermoelectric effect in bismuth has also been intensively investigated and large Seebeck coefficients of about 100 $\mu\text{V/K}$ were reported [20, 22]. One thus would wonder bismuth may also exhibit large SNE since it has large SOC. However, no theoretical nor experimental study on the SNE in bismuth has been reported so far. Therefore, we have carried out a systematic first-principles density functional theory (DFT) study on all the independent nonzero elements of the SHC and also the spin Nernst conductivity (SNC) of bismuth. In this paper, we present the main results of this systematic theoretical investigation. The rest of this paper is organized as follows. In the next section, we briefly describe the Berry phase formalism for calculating the intrinsic SHC and SNC of bismuth as well as the computational details. Section III consists of three subsections. We first present the calculated relativistic band structure of bismuth and also analyze its main features in Sec. III A. We then report the calculated spin Hall conductivity and corresponding estimated spin Hall angle in Sec. III B. We finally present the calculated spin Nernst conductivity and its temperature dependence as well as the estimated spin Nernst angles in Sec. III C. Finally, the conclusions drawn from this work are summarized in Sec. IV.

II. THEORY AND COMPUTATIONAL DETAILS

Bismuth crystallizes in a rhombohedral $R\bar{3}m$ structure (space group 166) with two Bi atoms per unit cell. [19] The experimental lattice constants and atomic positions measured at room temperature [19] are used in the present calculations. The electronic band structures are calculated based on the DFT with the generalized gradient approximation (GGA) to the exchange-correlation potential [41]. The accurate full-potential projector-augmented wave method [42], as implemented in the Vienna *ab initio* simulation package (VASP) [43, 44], is used. A large plane-wave cutoff energy of 400 eV is used in all the calculations. The self-consistent relativistic band structure calculation is performed with a Γ -centered k -point mesh of $16 \times 16 \times 16$ used in the Brillouin zone (BZ) integration by the tetrahedron method [45]. All the calculations are carried out with an energy convergence within 10^{-7} eV between the successive iteration.

The intrinsic SHC is calculated within the Berry phase formalism [10, 46]. In this approach, the SHC ($\sigma_{ij}^s = J_i^s/E_j$) is simply given by the BZ integration of the spin Berry curvature for all occupied bands [10],

$$\sigma_{ij}^s = e \sum_n \int_{BZ} \frac{d\mathbf{k}}{(2\pi)^3} f_{\mathbf{k}n} \Omega_{ij}^{n,s}(\mathbf{k}) \quad (1)$$

$$\Omega_{ij}^{n,s} = \sum_{n' \neq n} \frac{2Im[\langle \mathbf{k}n | \{\tau_s, v_i\} / 4 | \mathbf{k}n' \rangle \langle \mathbf{k}n' | v_j | \mathbf{k}n \rangle]}{(\epsilon_{\mathbf{k}n} - \epsilon_{\mathbf{k}n'})^2} \quad (2)$$

where J_i^s is the i th component of spin current density, $f_{\mathbf{k}n}$ is the Fermi function, and $\Omega_{ij}^{n,s}(\mathbf{k})$ is the spin Berry curvature for the n^{th} band at \mathbf{k} . $i, j = x, y, z$ and $i \neq j$. s denotes the spin direction, τ_s is the Pauli matrix, and v_i is the velocity operator [6]. Similarly, the spin Nernst conductivity ($\alpha_{ij}^s = -J_i^s/\nabla_j T$) can be written as [46, 47]

$$\alpha_{ij}^s = -\frac{1}{T} \sum_n \int_{BZ} \frac{d\mathbf{k}}{(2\pi)^3} \Omega_{ij}^{n,s}(\mathbf{k}) \times [(\epsilon_{\mathbf{k}n} - \mu) f_{\mathbf{k}n} + k_B T \ln(1 + e^{-\beta(\epsilon_{\mathbf{k}n} - \mu)})]. \quad (3)$$

In the SHC and SNC calculations, the velocity $\langle \mathbf{k}n' | v_i | \mathbf{k}n \rangle$ and spin velocity $\langle \mathbf{k}n | \{\tau_s, v_i\} / 4 | \mathbf{k}n' \rangle$ matrix elements are first calculated from the self-consistent relativistic band structures within the projector-augmented wave formalism [48] by using the VASP program. A homemade program [47, 49] is then used to calculate the spin Berry curvature [Eq. (2)] and also to perform the band summation and the BZ integration with the tetrahedron method [Eqs. (1) and (3)]. A very fine k -point mesh of about 124000 k -points in the BZ wedge is used, and this corresponds to the division of the ΓK line into $n_d = 40$ intervals. Further test calculations using denser k -point meshes of $n_d = 50$ and 60 show that the calculated SHC and SNC converge within a few percent.

III. RESULTS AND DISCUSSION

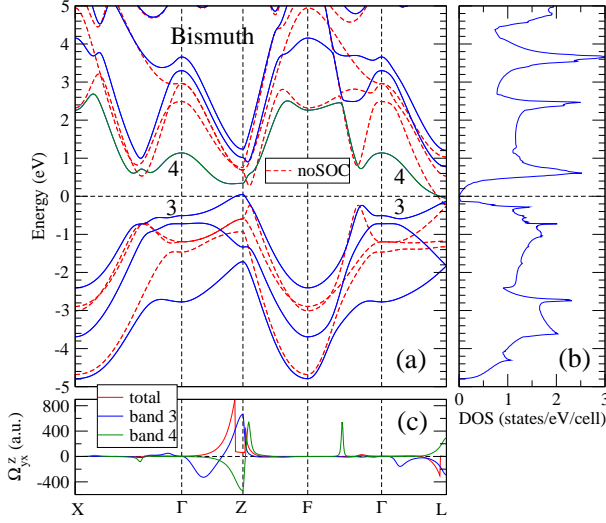


FIG. 1. (a) Relativistic band structure, (b) total density of states (DOS) and (c) total and band-resolved spin Berry curvatures (Ω_{yx}^{sz}) of bismuth semimetal. In (a), the scalar-relativistic band structure [i.e., without the spin-orbit coupling (SOC)] is also displayed for comparison (dashed red lines). The Fermi level is at 0 eV.

A. Electronic band structures

The calculated relativistic band structure and total density of states (DOSs) of bismuth are shown in Fig. 1(a) and Fig. 1(b), respectively. As reported earlier [21, 33], bismuth is a semimetal with a small DOS of 0.012 states/eV/cell at the Fermi level (E_F). Its Fermi surface consists of a small hole pocket at the Z point and three small electron pockets at the L point [Fig. 1(a)]. Top valence bands are made up of three broad Kramers-degenerate Bi p -orbital dominated bonding bands while bottom conduction bands consists of three broad Kramers-degenerate Bi p -orbital dominated antibonding bands. In Fig. 1(a), the scalar-relativistic band structure [i.e., calculated without the spin-orbit coupling (SOC) included] is also displayed. Figure 1(a) shows that including the SOC affects the band structure dramatically, as may be expected because bismuth has the largest atomic number (Z) and thus has perhaps the strongest SOC among the nonradioactive metals. For example, the gap between the top two valence bands at both the X and F points increases from 0.12 eV to 1.29 eV when the SOC is switched-on.

Interestingly, the E_F falls at the pseudogap (zero energy). Furthermore, the DOS increases steeply as energy (E) is lowered below E_F but increases much smoothly as E is raised just above the E_F . This strong electron-hole asymmetry in the DOS spectrum around E_F could

be the main reason why bismuth has the large negative Seebeck coefficients of $S_{xx} = -51 \mu\text{V/K}$ and $S_{zz} = -103 \mu\text{V/K}$ [20].

B. Spin Hall effect

As mentioned above, the SHC (σ_{ij}^s ; $s, i, j = x, y, z$) for a material is a third-order tensor. Nevertheless, for a highly symmetric crystal such as bismuth, most of the tensor elements are zero. As mentioned before, bismuth has a rhombohedral $R\bar{3}m$ structure with point group D_{3d} . [19] In Table I, the shape of the SHC tensor for Bi metal, uncovered by a symmetry analysis [50, 51], is displayed. Table I indicates that bismuth has only four nonzero independent elements, namely, σ_{yx}^z , σ_{xz}^y , σ_{zy}^x and σ_{xx}^y . Consequently, $\sigma_{yz}^x = -\sigma_{xz}^y$ and $\sigma_{zy}^x = -\sigma_{zx}^y$. The results of our first principles calculations are consistent with this symmetry analysis except that σ_{xx}^y is found to be zero, i.e., we have only three independent nonzero SHC elements (σ_{yx}^z , σ_{xz}^y and σ_{zy}^x). In Table II, all the three nonzero elements of the SHC of Bi are listed. The SHCs of previously studied heavy metals Pt, Au and Ta are also listed in Table II for comparison. Table II indicates that all three nonzero SHC elements of Bi are large. In particular, σ_{yx}^z is 1062 (\hbar/e)(S/cm), being about half that of fcc Pt which possesses the largest intrinsic SHC (~ 2140 (\hbar/e)(S/cm)) among the elemental metals [10, 49]. Furthermore, all three SHC elements are more than two times larger than that of Au and Ta (Table II).

Interestingly, Bi semimetal exhibits anisotropic SHE. For an isotropic cubic metal (e.g., Pt), there is only one independent SHC element, namely, $\sigma_{yx}^z = \sigma_{xz}^y = \sigma_{zy}^x$. In a hcp metal (e.g., Zr), however, $\sigma_{yx}^z \neq \sigma_{xz}^y$ although $\sigma_{zy}^x = \sigma_{zx}^y$. [40] Thus, one can define the SHC anisotropy as $\Delta_{zy}^{sH} = \sigma_{yx}^z - \sigma_{xz}^y$ [40]. For rhombohedral bismuth, $\sigma_{yx}^z \neq \sigma_{xz}^y \neq \sigma_{zy}^x$ (see Table I), and consequently, the SHC anisotropy should be characterized by two parameters, namely, $\Delta_{zy}^{sH} = \sigma_{yx}^z - \sigma_{xz}^y$ and $\Delta_{yx}^{sH} = \sigma_{xz}^y - \sigma_{zy}^x$. Table II indicates that Bi semimetal shows significantly anisotropic spin Hall effect, although its rhombohedral structure can be considered as a superposition of two very slightly distorted fcc lattices of Bi atoms [19]. Specifically, Table II indicates that $\Delta_{zy}^{sH} = 159$ (\hbar/e)(S/cm), meaning that when the polarization of the spin current is switched from the z direction to the y direction, the SHC would get reduced by about 15 %. On the other hand, $\Delta_{yx}^{sH} = -64$ (\hbar/e)(S/cm) suggest that the SHC would be increased by about 7 % if the spin polarization is further rotated from the y axis to the x axis. As for the large anisotropic g factor of holes in bismuth [25], this significant crystalline anisotropy in the SHE of Bi semimetal could be attributed to its peculiar band structure near the Fermi level and also its large SOC.

We notice that for the application of SHE in spintronics such as spin-orbit torque switching-based nanodevices [13, 14], the crucial quantity is the so-called spin Hall angle Θ_{sH} which characterizes the charge-to-

TABLE I. $R\bar{3}m$ symmetry-imposed shape of the spin Hall conductivity (σ) and spin Nernst conductivity (α) tensors [50, 51]. Here $Z = \sigma$ or α . Note that there are only four nonzero independent matrix elements, namely, Z_{yx}^z , Z_{xz}^y , Z_{zy}^x and Z_{xx}^y .

$$\begin{array}{ccc} \underline{Z}^x & \underline{Z}^y & \underline{Z}^z \\ \hline \begin{pmatrix} 0 & Z_{xx}^y & 0 \\ Z_{xx}^y & 0 & -Z_{xz}^y \\ 0 & Z_{zy}^x & 0 \end{pmatrix} & \begin{pmatrix} Z_{xx}^y & 0 & Z_{xz}^y \\ 0 & -Z_{xx}^y & 0 \\ -Z_{zy}^x & 0 & 0 \end{pmatrix} & \begin{pmatrix} 0 & -Z_{yx}^z & 0 \\ Z_{yx}^z & 0 & 0 \\ 0 & 0 & 0 \end{pmatrix} \\ \hline \end{array}$$

TABLE II. Calculated spin Hall conductivity (SHC) (σ_{yx}^z , σ_{xz}^y and σ_{zy}^x), and spin Nernst conductivity (SNC) (α_{yx}^z , α_{xz}^y and α_{zy}^x) at room temperature of Bi semimetal. Previous results for some $5d$ metals (Pt, Au and β -Ta) are also listed for comparison. To estimate spin Hall (Nernst) angle $\Theta_{sH} = 2\sigma^s/\sigma_0$ ($\Theta_{sN} = 2\alpha^s/\alpha_0 = \alpha^s/S_0/\sigma_0$), we also list experimental electrical conductivity σ_0 and Seebeck coefficient S_0 as well as the estimated Θ_{sH} and Θ_{sN} . Note that the calculated SHC σ_{xx}^y and SNC α_{xx}^y are zero (within the numerical uncertainty) and thus are not listed here. The energy derivatives of the σ_{yx}^z , σ_{xz}^y and σ_{zy}^x at the Fermi level are 200, -659, -276 ($\frac{\hbar}{e} \frac{1}{\Omega \text{cm}}$), respectively.

| System | σ_{xx} (σ_{zz}) ($\frac{10^4}{\Omega \text{cm}}$) | S_{xx} (S_{zz}) ($\frac{\mu V}{K}$) | σ_{yx}^z ($\frac{\hbar}{e} \frac{1}{\Omega \text{cm}}$) | Θ_{sH}^z (%) | σ_{xz}^y (σ_{zy}^x) ($\frac{\hbar}{e} \frac{1}{\Omega \text{cm}}$) | $\Theta_{sH,xz}^y$ ($\Theta_{sH,zy}^x$) (%) | α_{yx}^z ($\frac{\hbar}{e} \frac{A}{mK}$) | Θ_{sN}^z (%) | α_{xz}^y (α_{zy}^x) ($\frac{\hbar}{e} \frac{A}{mK}$) | $\Theta_{sN,xz}^y$ ($\Theta_{sN,zy}^x$) (%) |
|-------------|--|--|--|---------------------------|---|--|---|------------------------|---|--|
| Bi | 0.90 (0.75) ^a | -51 (-103) ^a | 1062, 474 ^b ~600 ^c 500~1000 ^f | 24.0 0~24 ^d | 903 (967) | 22 (23) 0~24 ^d , 17 ^e | -0.139 | 0.61 | 0.349 (0.180) | -1.01 (-0.57) |
| Pt | 20.8 ^g | -3.7 ^h | 2139 ⁱ 2280 ^k | 10 ^g | — | — | -1.09 ^j -1.57 ^h | -20 ^h | — | — |
| Au | 9.1 ^g | 1.5 ^l | 446 ^m | 1.4 ⁿ | — | — | 0.13 ^o | 1.8 | — | — |
| β -Ta | 0.29 ^g | -1.5 ^p | -378 ^m , -389 ^k -400 ^q | -1.0 ⁿ | — | — | 0.71 ^o | — | — | — |

^aExperiment at 300 K [20]; ^bTight-binding Hamiltonian calculation [33]; ^cExperiment on Bi_{1-x}Sb_x with $x \leq 0.35$ [52];

^dExperiments (see [38] and references therein); ^eExperiment [53]; ^fExperiment [32]; ^gExperiment [54]; ^hExperiment at 255 K [17]; ⁱ*Ab initio* calculation [10]; ^j*Ab initio* calculation [47]; ^k*Ab initio*-based Wannier interpolation [55]; ^lExperiment [56]; ^m*Ab initio* calculation [57, 58]; ⁿExperiment at 300 K [58]; ^oThis work; for computational details, see [58]; ^pExperiment at 300 K [59]; ^qExperiment [12].

spin conversion efficiency. The spin Hall angle is given by $\Theta_{sH} = (2e/\hbar)J^s/J^c = 2\sigma^s/\sigma^c$ where J^c and σ^c are the longitudinal charge current density and conductivity, respectively (see, e.g., Refs. [14] and [60]). Since bismuth has an electrical conductivity much smaller than that of Pt and Au (Table II), we would expect that the Θ_{sH} values for all the nonzero SHC elements should be much larger than Au and also larger than Pt. Indeed, using the measured electrical conductivity for Bi, we find that the Θ_{sH} values for σ_{yx}^z , σ_{xz}^y and σ_{zy}^x are 24 %, 22 % and 23 %, respectively. These values are significantly larger than that of Pt and Au (see Table II).

Since the SHC could be sensitive to the location of the Fermi energy (E_F) [6, 10, 49], we also calculate the SHC as a function of E_F within the so-called rigid band approximation, i.e., only the Fermi energy is varied while the band structure is kept fixed. The results may allow us to optimize the SHC of Bi by chemical doping or gating. However, we should note that shifting the Fermi level by, e.g., chemical doping will inevitably change the band structure. If these changes in the band structure are large, they will render the rigid band approximation invalid. Nonetheless, if the amount of hole or electron doping is small, one may expect that the band structure

is hardly affected and hence the predictions are valid. The obtained spectra of the SHC elements are displayed Fig. 2. Indeed, as one can see from Fig. 2, the SHC curves show a significant dependence on the E_F . In particular, all three elements have a prominent peak near the E_F with the peak values being as large as about 1000 (\hbar/e)(S/cm) [see Fig. 2(a)]. This could be attributed to the fact that the Fermi level falls within the narrow band gaps around the Z and L points in the BZ [Fig. 1(a)]. This is reminiscent of platinum metal where the SHC also exhibits a prominent peak at the E_F which falls within the SOC-induced band gaps [10]. It was pointed out in [10] that when two degenerate bands become slightly gapped by the SOC, a pair of large peaks of spin Berry curvature with opposite signs would appear on the occupied and empty bands, respectively, thus resulting in a gigantic contribution to the SHC [see Eq. (2)]. Indeed, Fig. 3(c) indicates that spin Berry curvatures Ω_{yx}^z of bands 3 and 4 peak in the vicinity of the Z and L points with large magnitudes but opposite signs. Since band 3 is almost full while band 4 is nearly empty [Fig. 1(a)], the total Ω_{yx}^z shows a gigantic positive peak near the Z point along the Γ -Z line and also a smaller negative peak near the L point along the Γ -L line. Clearly, the large

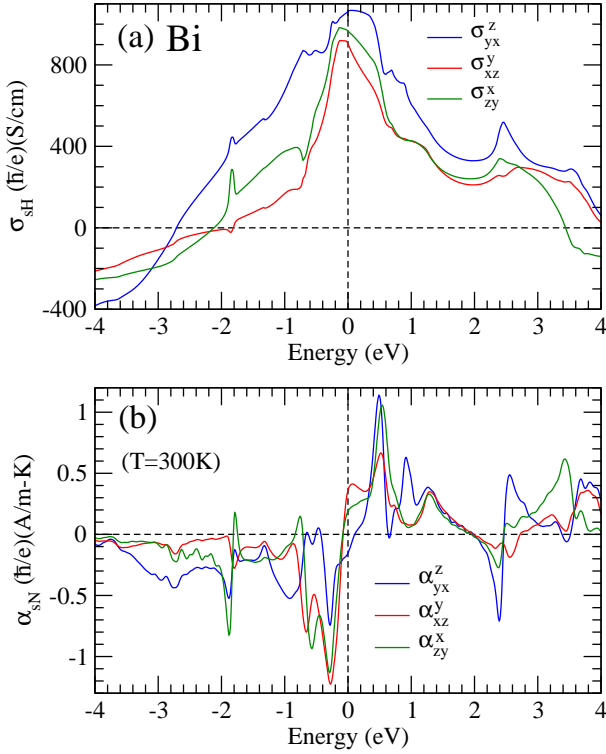


FIG. 2. (a) Spin Hall conductivity and (b) spin Nernst conductivity at $T = 300$ K as a function of the Fermi level of Bi semimetal.

positive σ_{yx}^z peak near the E_F results from the gigantic Ω_{yx}^z near the Z point [Fig. 1(c)].

As the energy is either raised above the E_F or lowered below the E_F , the magnitudes of all three elements decrease monotonically [Fig. 2(a)]. Interestingly, the anisotropy in the SHE gets considerably enhanced. For example, when the E_F is shifted upwards by 0.20 eV, the magnitudes of the Δ_{zy}^{sH} and Δ_{yx}^{sH} would almost be doubled, changing to 280 (\hbar/e)(S/cm) and -120 (\hbar/e)(S/cm), respectively. This can be easily achieved by electron doping of 0.009 e/unit cell (or $n_e = 1.3 \times 10^{20} \text{ cm}^{-3}$) via substitutional alloying $\text{Bi}_{1-x}\text{Te}_x$ [32]. Similarly, if the E_F is lowered by 0.35 eV, the magnitudes of the Δ_{zy}^{sH} and Δ_{yx}^{sH} would also be nearly doubled, changing to 289 (\hbar/e)(S/cm) and -133 (\hbar/e)(S/cm), respectively. This can be accomplished by hole doping of 0.190 e/unit cell (or $n_h = 2.7 \times 10^{21} \text{ cm}^{-3}$) via substitutional alloying $\text{Bi}_{1-x}\text{Sn}_x$ [32]. At around -2.0 eV, σ_{xz}^y and σ_{zy}^x change sign while σ_{yx}^z changes sign at about -2.7 eV. Figure 2(a) shows that in the energy range from -2.0 to -0.5 eV, there is a prominent difference between σ_{xz}^y and σ_{zy}^x , thus indicating a strongly anisotropic SHE. For example, Δ_{zy}^{sH} is as large as 637 (\hbar/e)(S/cm) at -0.72 eV [Fig. 2(a)].

As mentioned before, one group reported the realistic tight-binding Hamiltonian calculation of the intrinsic SHC for Bi. Nevertheless, only one independent element (σ_{yx}^z) was calculated. [33] Overall, the shape of the $\sigma_{yx}^z(E)$ spectrum reported in [33] agrees well with that

displayed in Fig. 2(a). However, Table II indicates that the σ_{yx}^z value [472 (\hbar/e)(S/cm)] reported in [33] is more than two times smaller than that [1062 (\hbar/e)(S/cm)] of the present calculation. We are unable to understand the origin of this big discrepancy between the two calculations since we do not know the details of the previous calculation [33]. Nevertheless, we do notice that our calculated SHC values for fcc Pt and β -Ta (Table II) agree very well with the previous independent calculations using the different methods [10, 55, 61] (see Table II).

As noted above, the magnitude of the reported Θ_{sH} values varies from zero (negligibly small) to 24 %, depending on the spin current detection method and also the magnetic material used to inject spin current in the experiments [34–39, 53]. Such a wide range of the measured Θ_{sH} values could also suggest that there may be significant contributions from the extrinsic mechanisms such as the side-jump and skew scattering [13, 14], which would depend on the quality of the samples used in the experiments. Also, we notice that the Bi films used in the experiments were deposited on different substrates and consequently, the substrate-dependent charge transfer may occur. Because both the magnitude and anisotropy of the SHC are sensitive to carrier doping [see Fig. 2(a)], this could be another reason why the reported Θ_{sH} values differ significantly from each other. Since the spin Hall angle also depends on the electric conductivity, it would be better to compare the experimentally determined and theoretically calculated SHC. In this context, we notice that the measured SHC for $\text{Bi}_{1-x}\text{Sb}_x$ with $x \leq 0.35$ is 600 (\hbar/e)(S/cm) [52]. Very recently, the SHC of 500~1000 (\hbar/e)(S/cm) in pure bismuth was also reported [32]. These experimental SHC values are quite close to our theoretical SHC values (Table II). Furthermore, the SHC of the doped bismuth as a function of carrier concentration was reported [32], which exhibits a pronounced peak at pure bismuth, agreeing well with the SHC versus E_F curves displayed in Fig. 2(a). We hope that our interesting finding of anisotropic and tunable spin Hall conductivity and angle would spur further experiments on the SHE in bismuth semimetal using single crystal specimens.

C. Spin Nernst effect

The SNC (α_{ij}^s) for a solid is also a third-order tensor. Since the transverse spin currents generated by a longitudinal electric field and a longitudinal temperature gradient have the same transformation properties under the symmetry operations, the shape of the SNC is identical to that of the SHC [50] (see Table I). Therefore, the SNC of bismuth semimetal also has only three nonzero independent elements, namely, α_{yx}^z , α_{xz}^y , and α_{zy}^x . Table II shows that the calculated values of these nonzero elements of the SNC tensor $T = 300$ K are rather significant. In fact, they are in the same order of magnitude as that of gold metal (Table II). Nevertheless, they are a

few times smaller than that of platinum metal.

Interestingly, Table II indicates that the SNC of Bi is more anisotropic than the SHC. First of all, in contrast to σ_{yx}^z and σ_{zy}^x , α_{yx}^z and α_{xz}^y have opposite signs. The magnitude of α_{xz}^y is nearly three times larger than that of α_{yx}^z . This gives rise to the large anisotropic parameter $\Delta_{zy}^{sN} = \alpha_{yx}^z - \alpha_{xz}^y = 0.49$ (\hbar/e)(A/m-K), indicating that when the spin polarization is switched from the z axis to the y axis, the SNC would not only change sign but also get enhanced by a factor of ~ 3 . On the other hand, we notice that $\alpha_{zy}^x = 0.18$ (\hbar/e)(A/m-K), meaning that the SNC would be reduced by half if the spin polarization is further rotated from the y axis to the x axis.

As for the SHC, we also calculate the three elements of the SNC as a function of E_F . In Fig. 2(c), all the three SNC elements (α_{yx}^z , α_{xz}^y and α_{zy}^x) at $T = 300$ K are displayed as a function of E_F . Furthermore, we note that in the low temperature limit, Eq. (3) can be written as the Mott relation,

$$\alpha_{ij}^s(E_F) = -\frac{\pi^2}{3} \frac{k_B^2 T}{e} \sigma_{ij}^s(E_F)', \quad (4)$$

which indicates that the SNC is proportional to the energy derivative of the SHC at the E_F . In other words, a peak in the SNC would occur when the SHC has a steep slope. Interestingly, the Mott relation shows the reason that α_{yx}^z is negative while α_{xz}^y and α_{zy}^x are positive [see Table II and Fig. 2(b)], is because the slope of σ_{yx}^z is positive while the slopes of σ_{xz}^y and σ_{zy}^x are negative [see Fig. 2(a)].

Figure 2(c) clearly shows that the SNC has a stronger E_F dependence than the SHC. Remarkably, both α_{xz}^y and α_{zy}^x decreases sharply as the energy is lowered from the E_F and change sign at -0.08 eV and then reaches its minimum of -1.22 (\hbar/e)(A/m-K) at -0.28 eV when the energy is further lowered [see Fig. 2(c)]. Note that hole doping of merely 0.001 and 0.108 e per unit cell, respectively, would realize the sign change and also reach the maximal magnitude. The Mott relation clearly indicates that this is caused by the rapid change of the slope of the corresponding SHC elements in this energy region. On the other hand, when the energy increases, the α_{yx}^z increases steadily, changes sign at ~ 0.11 eV and then reaches its maximum of 1.14 (\hbar/e)(A/m-K) at 0.49 eV, which can be obtained by electron-doping of 0.122 e per unit cell. Note again that the peak is located at the point where σ_{xy}^z drops sharply [Fig. 2(a)], being consistent with the Mott relation.

We also calculate the three independent elements of the SNC as a function of T , as displayed in Fig. 3. Figure 3 shows that α_{xz}^y and α_{zy}^x are positive while α_{yx}^z is negative in the entire considered temperature range. The magnitude of all the three elements increases monotonically with T . In the low temperature region (e.g., $T \leq 200$ K), all the elements are roughly proportional to T , as indicated by the Mott relation [Eq. (4)]. Using the calculated energy derivatives of the SHC elements (Table II) and Eq. (4), we can estimate the SNC elements at a

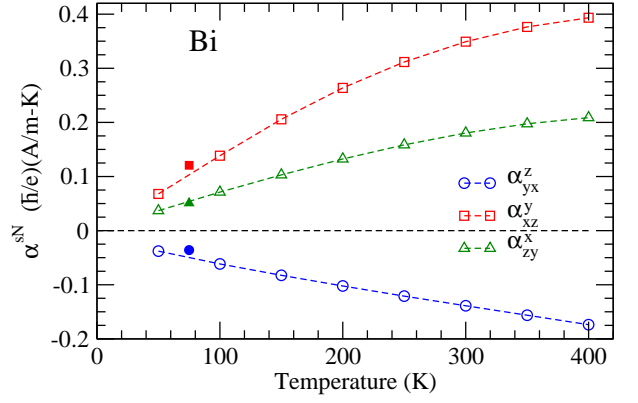


FIG. 3. Spin Nernst conductivity (SNC) (α_{yx}^z , α_{xz}^y and α_{zy}^x) of Bi semimetal as a function of temperature. The solid symbols denote the SNC values estimated using the energy derivatives of the SHC at the E_F (see Table II) and the Mott relation [Eq. (4)].

low temperature. Indeed, Fig. 3 indicates that such estimated values of the SNC elements at 75 K agree quite well with that of the full calculation using Eq. (3), verifying that the Mott relation holds quantitatively at low temperatures.

Finally, from the viewpoint of the application of SNE in spin caloritronics, the key quantity is the spin Nernst angle Θ_{sN} which measures the heat-to-spin conversion efficiency and is given by $\Theta_{sN} = (2e/\hbar)J^s/J^h = 2\alpha^s/\alpha^L$ where J^h and α^L are the longitudinal heat current density and Nernst coefficient, respectively [17]. Here $\alpha^L = S_{aa}\sigma_{aa}$ where S_{aa} is the Seebeck coefficient. Using the measured σ_{xx} (σ_{zz}) and S_{xx} (S_{zz}) as well as the calculated α^s of bismuth semimetal (Table II), we estimate the Θ_{sN} values and list the results in Table II. The obtained Θ_{sN} values are around 1 %, which are significant. Nevertheless, they are more than ten times smaller than that (-20 %) of Pt metal [17]. This is because not only the Seebeck coefficients of Bi semimetal are much larger than that of Pt metal but also the calculated SNC values of Bi are several times smaller than that of Pt (see Table II).

IV. CONCLUSIONS

Summarising, we have performed a thorough theoretical study of the SHE and SNE in bismuth based first-principles relativistic band structure calculations and the Berry phase formalism. Our symmetry analysis indicates that unlike cubic metals such as Pt and Au, the SHC and SNC tensors have three independent nonzero elements, viz., Z_{yx}^z , Z_{xz}^y and Z_{zy}^x . We have calculated all the three elements as a function of the Fermi energy (E_F), instead of one element in the previous calculation [33]. The results of these calculations show that all SHC tensor elements are large, being ~ 1000 (\hbar/e)(S/cm). They are comparable to that of platinum which possesses the

largest intrinsic SHC among the metals. Furthermore, because bismuth semimetal has low electrical conductivity, the corresponding spin Hall angles are gigantic, being $\sim 20\%$ (see Table II) and much larger than that of platinum (Table II). All the calculated SNC tensor elements are also pronounced, being comparable to that $[\sim 0.13 (\hbar/e)(\text{A/m-K})]$ of gold, although they are several times smaller than that of platinum. Both the magnitude and sign of all the calculated conductivity elements vary strongly with the Fermi level (Fig. 2), indicating that the SHE and SNE in bismuth could be optimized by varying the Fermi level via, e.g., chemical doping. All these suggest that bismuth is a promising material for spintronics and spin caloritronics. Interestingly, in contrast to Pt and Au where $Z_{yx}^z = Z_{xz}^y = Z_{zy}^x$, the SHE and SNE in bismuth are anisotropic, i.e., Z_{yx}^z , Z_{xz}^y and Z_{zy}^x differ significantly. In particular, α_{yx}^z and α_{xz}^y even differ in sign. Consequently, the Hall voltages due to the inverse SHE and inverse SNE from the different conductivity elements

could cancel each other and thus result in a small spin Hall angle if polycrystalline samples are used, which may explain why the measured spin Hall angles ranging from nearly 0 to 25 % have been reported. We thus believe that this work would stimulate further spin current experiments on bismuth using highly oriented single crystal specimens.

ACKNOWLEDGMENTS

The author thanks Prof. Chia Ling Chien for many enlightening discussions and advices on magnetism, superconductivity and spin-related transports in general as well as on the fascinating properties of bismuth semimetal in particular over the years. The author acknowledges the support from the Ministry of Science and Technology and the National Center for Theoretical Sciences, Taiwan.

-
- [1] M. I. D'yakonov and V. I. Perel, Spin orientation of electrons associated with the interband absorption of light in semiconductors, *Sov. Phys. JETP* **33**, 1053 (1971).
 - [2] J. E. Hirsch, Spin Hall effect, *Phys. Rev. Lett.* **83**, 1834 (1999).
 - [3] S. Murakami, N. Nagaosa, and S.-C. Zhang, Dissipationless quantum spin current at room temperature, *Science* **301**, 1348 (2003).
 - [4] J. Sinova, D. Culcer, Q. Niu, N. A. Sinitsyn, T. Jungwirth, and A. H. MacDonald, Universal intrinsic spin Hall effect, *Phys. Rev. Lett.* **92**, 126603 (2004).
 - [5] Y. K. Kato, R. C. Gossard and D. D. Awschalom, Observation of the spin Hall effect in semiconductors, *Science* **306**, 1910 (2004).
 - [6] G. Y. Guo, Y. Yao and Q. Niu, *Ab initio* calculation of the intrinsic spin Hall effect in semiconductors, *Phys. Rev. Lett.* **94**, 226601 (2005).
 - [7] E. Saitoh, M. Ueda, H. Miyajima and G. Tatara, Conversion of spin current into charge current at room temperature: inverse spin-Hall effect, *Appl. Phys. Lett.* **88**, 182509 (2006).
 - [8] S. O. Valenzuela and M. Tinkham, Direct electronic measurement of the spin Hall effect, *Nature* **442**, 176 (2006).
 - [9] T. Kimura, Y. Otani, T. Sato, S. Takahashi and S. Maekawa, Room-temperature reversible spin Hall effect, *Phys. Rev. Lett.* **98**, 156601 (2007).
 - [10] G. Y. Guo, S. Murakami, T.-W. Chen, and N. Nagaosa, Intrinsic Spin Hall Effect in Platinum: First-Principles Calculations, *Phys. Rev. Lett.* **100**, 096401 (2008).
 - [11] T. Tanaka, H. Kontani, M. Naito, D. S. Hirashima, K. Yamada, and J. Inoue, Intrinsic spin Hall effect and orbital Hall effect in 4 and 5 transition metals, *Phys. Rev. B* **77**, 165117 (2008).
 - [12] L. Liu, C.-F. Pai, Y. Li, H.-W. Tseng, D. C. Ralph, and R. A. Buhrman, Spin-Torque Switching with the Giant Spin Hall Effect of Tantalum, *Science* **336**, 555 (2012).
 - [13] A. Hoffmann, Spin Hall effects in metals, *IEEE Trans. Mag.* **49**, 5172 (2013).
 - [14] J. Sinova, S. O. Valenzuela, J. Wunderlich, C. H. Back and T. Jungwirth, Spin Hall effects, *Rev. Mod. Phys.* **87**, 1213 (2015).
 - [15] S. Cheng, Y. Xing, Q.-F. Sun, and X. C. Xie, Spin Nernst effect and Nernst effect in two-dimensional electron systems, *Phys. Rev. B* **78**, 045302 (2008).
 - [16] G. E. W. Bauer, E. Saitoh, and B. J. van Wees, Spin caloritronics, *Nat. Mater.* **11**, 391 (2012).
 - [17] S. Meyer, Y.-T. Chen, S. Wimmer, M. Althammer, T. Wimmer, R. Schlitz, S. Geprägs, H. Huebl, D. Ködderitzsch, H. Ebert, G. E. W. Bauer, R. Gross, and S. T. B. Goennenwein, Observation of the spin Nernst effect, *Nat. Mater.* **16**, 977 (2017).
 - [18] P. Sheng, Y. Sakuraba, Y.-C. Lau, S. Takahashi, S. Mitani, and M. Hayashi, The spin Nernst effect in tungsten, *Sci. Adv.* **3**, e1701503 (2017).
 - [19] P. Cucka and C. S. Barrett, The Crystal structure of Bi and of solid solutions of Pb, Sn, Sb and Te in Bi, *Acta Cryst.* **15**, 865 (1962).
 - [20] C. F. Gallo, B. S. Chandrasekhar, and P. H. Sutter, Transport properties of bismuth single crystals, *J. Appl. Phys.* **34**, 144 (1963).
 - [21] Y. Liu and R. E. Allen, Electronic structure of the semimetals Bi and Sb, *Phys. Rev. B* **52**, 1566 (1995).
 - [22] T. J. Seebeck, Magnetische Polarisation der Metalle und Erze durch Temperature-Differenz, *Abhandlungen der physikalischen Klasse der Königlich Preussischen Akademie der Wissenschaften zu Berlin* **1822-1823**, 265 (1825).
 - [23] H. Kamerlingh-Onnes and B. Beckman, *Comm. Phys. Lab. Leiden* **129a**, 3 (1912).
 - [24] P. Kapitza, *Proc. Roy. Soc. A* **129a**, 358 (1928).
 - [25] Y. Fuseya, Z. Zhu, B. Fauque, W. Kang, B. Lenoir and K. Behnia, Origin of the large anisotropic g factor of holes in bismuth, *Phys. Rev. Lett.* **115**, 216401 (2015).
 - [26] O. Prakash, A. Kumar, A. Thamizhavel, and S. Ramakrishnan, Evidence for bulk superconductivity in pure bismuth single crystals at ambient pressure, *Science* **355**, 52 (2017).

- [27] F. Schindler, Z. Wang, M. G. Vergniory, A. M. Cook, A. Murani, S. Sengupta, A. Y. Kasumov, R. Deblock, S. Jeon, I. Drozdov, H. Bouchiat, S. Gueron, A. Yazdani, B. A. Bernevig and T. Neupert, Higher-order topology in bismuth, *Nature Physics* **14**, 918 (2018).
- [28] C.-H. Hsu, X. Zhou, T.-R. Chang, Q. Ma, N. Gedik, A. Bansil, S.-Y. Xu, H. Lin and L. Fu, Topology on a new facet of bismuth, *PNAS* **116**, 13255 (2019).
- [29] Y. Fuseya, M. Ogata and H. Fukuyama, Spin-Hall effect and diamagnetism of Dirac electrons, *J. Phys. Soc. Jpn* **81**, 093704 (2012).
- [30] Y. Fuseya, M. Ogata and H. Fukuyama, Spin-Hall effect and diamagnetism of Anisotropic Dirac electrons in solids, *J. Phys. Soc. Jpn* **83**, 074702 (2014).
- [31] Y. Fuseya, M. Ogata and H. Fukuyama, Transport properties and diamagnetism of Dirac electrons in bismuth, *J. Phys. Soc. Jpn* **84**, 012001 (2015).
- [32] Z. Chi, G. Qu, Y.-C. Lau, M. Kawaguchi, J. Fujimoto, K. Takanashi, M. Ogata and M. Hayashi, Spin Hall effect driven by the spin magnetic moment current in Dirac materials, *Phys. Rev. B* **105**, 214419 (2022).
- [33] C. Sahin and E. Flatte, Tunable giant spin Hall conductivities in a strong spin-orbit semimetal: $\text{Bi}_{1-x}\text{Sb}_x$, *Phys. Rev. Lett.* **114**, 107201 (2015).
- [34] D. Hou, Z. Qiu, K. Harii, Y. Kajiwara, K. Uchida, Y. Fujikawa, H. Nakayama, T. Yoshino, T. An, K. Ando, X. F. Jin and E. Saitoh, Interface induced inverse spin Hall effect in bismuth/permalloy bilayer, *Appl. Phys. Lett.* **101**, 042403 (2012).
- [35] H. Emoto, Y. Ando, G. Eguchi, R. Ohshima, E. Shikoh, Y. Fuseya, T. Shinjo and M. Shiraishi, Transport and spin conversion of multicarriers in semimetal bismuth, *Phys. Rev. B* **93**, 174428 (2016).
- [36] H. J. Zhang, S. Yamamoto, B. Gum H. Li, M. Maekawa, Y. Fukaya and A. Kawasuso, Charge-to-spin conversion and spin diffusion in Bi/Ag bilayers observed by spin polarized positron beam, *Phys. Rev. Lett.* **114**, 166602 (2015).
- [37] D. Yue, W. Lin, J. Li, X.-F. Jin and C. L. Chien, Spin-to-charge conversion in Bi films and Bi/Ag bilayers, *Phys. Rev. Lett.* **121**, 037201 (2018).
- [38] D. Yue, W. Lin and C. L. Chien, Negligible spin-charge conversion in Bi films and Bi/Ag(Cu) bilayers, *APL Mater.* **9**, 050904 (2021).
- [39] S. Sangiao, J. I. Morales-Aragones, I. Lucas, P. Jimenez-Cavero, L. Morellon, C. Sanchez-Azqueta and J. M. De Teresa, Optimization of YIG/Bi stacks for spin-to-charge conversion and influence of aging, *J. Phys. D: Appl. Phys.* **54**, 375305 (2021).
- [40] F. Freimuth, S. Blügel and Y. Mokrousov, Anisotropic spin Hall effect from first principles, *Phys. Rev. Lett.* **105**, 246602 (2010).
- [41] J. P. Perdew, K. Burke, and M. Ernzerhof, Generalized Gradient Approximation Made Simple, *Phys. Rev. Lett.* **77**, 3865 (1996).
- [42] P. E. Blöchl, Projector augmented-wave method, *Phys. Rev. B* **50**, 17953 (1994).
- [43] G. Kresse and J. Furthmüller, Efficient iterative schemes for *ab initio* total-energy calculations using a plane-wave basis set, *Phys. Rev. B* **54**, 11169 (1996).
- [44] G. Kresse and J. Hafner, *Ab initio* molecular dynamics for liquid metals, *Phys. Rev. B* **47**, 558 (1993).
- [45] W. M. Temmerman, P. A. Sterne, G. Y. Guo and Z. Szotek, Electronic Structure Calculations of High Tc Materials, *Molecular Simulations* **4**, 153 (1989).
- [46] D. Xiao, M.-C. Chang, and Q. Niu, Berry phase effects on electronic properties, *Rev. Mod. Phys.* **82**, 1959 (2010).
- [47] G.-Y. Guo and T.-C. Wang, Large anomalous Nernst and spin Nernst effects in the noncollinear antiferromagnets Mn_3X (X=Sn, Ge, Ga), *Phys. Rev. B* **96**, 224415 (2017); *Phys. Rev. B* **100**, 169907 (E) (2019).
- [48] B. Adolph, J. Furthmüller and F. Beckstedt, Optical properties of semiconductors using projector-augmented waves, *Phys. Rev. B* **63**, 125108 (2001).
- [49] G. Y. Guo, Q. Niu and N. Nagaosa, Anomalous Nernst and Hall effects in magnetized platinum and palladium, *Phys. Rev. B* **89**, 214406 (2014).
- [50] M. Seemann, D. Kodderitzsch, S. Wimmer, and H. Ebert, Symmetry-imposed shape of linear response tensors, *Phys. Rev. B* **92**, 155138 (2015).
- [51] S. V. Gallego, J. Etxebarria, L. Elcoro, E. S. Tasci, and J. M. Perez-Mato, Automatic calculation of symmetry-adapted tensors in magnetic and non-magnetic materials: a new tool of the Bilbao Crystallographic Server, *Acta Cryst.* **A75**, 438 (2019).
- [52] Z. Chi, Y.-C. Lau, X. Xu, T. Ohkubo, K. Hono and M. Hayashi, The spin Hall effect of Bi-Sb alloys driven by thermally excited Dirac-like electrons, *Sci. Adv.* **6**, eaay2324 (2020).
- [53] N. Fukumoto, R. Ohshima, M. Aoki, Y. Fuseya, M. Matsushima, E. Shigematsu, T. Shinjo, Y. Ando, S. Sakamoto, Masanobu Shiga, S. Miwa and M. Shiraishi, Observation of gigantic spin conversion anisotropy in bismuth, *arXiv: 2208.00589* (2022).
- [54] H. L. Wang, C. H. Du, Y. Pu, R. Adur, P. C. Hammel and F. Y. Yang, Scaling of spin Hall angle in 3d, 4d, 5d metals from $\text{Y}_3\text{Fe}_5\text{O}_{12}$ /metal spin pumping, *Phys. Rev. Lett.* **112**, 197201 (2014).
- [55] J. Qiao, J. Zhou, Z. Yuan, W. Zhao, Calculation of intrinsic spin Hall conductivity by Wannier interpolation, *Phys. Rev. B* **98**, 214402 (2018).
- [56] P. Zolotavin, C. I. Evans and D. Natelson, Substantial local variation of the Seebeck coefficient in gold nanowires, *Nanoscale* **9**, 9160 (2017).
- [57] G. Y. Guo, *Ab initio* calculation of intrinsic spin Hall conductivity of Pd and Au, *J. Appl. Phys.* **105**, 07C701 (2009).
- [58] D. Qu, S. Y. Huang, G. Y. Guo and C. L. Chien, Inverse spin Hall effect in $\text{Au}_x\text{Ta}_{1-x}$ alloy films, *Phys. Rev. B* **97**, 024402 (2018).
- [59] P. Fiftis, L. Kirsch, D. Andruczyk, D. Curreli and D. N. Ruzic, Seebeck coefficient measurements on Li, Sn, Ta, Mo, and W, *J. Nuc. Mater.* **438**, 224 (2013).
- [60] J.-C. Tung and G.-Y. Guo, High spin polarization of the anomalous Hall current in Co-based Heusler compounds, *New J. Phys.* **15**, 033014 (2013).
- [61] J. H. Ryoo, C.-H. Park and I. Souza, Computation of spin Hall conductivities from first-principles by maximally localized Wannier functions, *Phys. Rev. B* **99**, 214402 (2019).